


# Origin of layer-dependent electrical conductivity of transition metal dichalcogenides

Akash Singh, Manoj Dey, and Abhishek Kumar Singh <sup>\*</sup>*Materials Research Centre, Indian Institute of Science, Bangalore 560012, India*

(Received 22 September 2021; revised 10 April 2022; accepted 12 April 2022; published 26 April 2022)

Transition metal dichalcogenide (TMD) shows layer-dependent electrical conductivity. However, there are conflicting experimental reports on the trend of conductivity, which is attributed to originating from point defects as a function of the number of layers (NLs). Using density functional theory, we analyze the layer-dependent defect thermodynamics of *n*- and *p*-type defects in MoS<sub>2</sub> and WS<sub>2</sub>. The shallow donor levels of hydrogen defects systematically become deep with the increasing NLs to six or seven-layers and hence reduces the *n*-type conductivity. Moreover, the deep acceptor  $V_S$  in a one-layer turns into a weak shallow acceptor for six-layers. Interestingly, from eight-layers onwards, the thermodynamic defect transition levels shift towards the conduction band due to the interplay between the bonding characteristic of the localized defect state and Coulombic repulsion of the added charge in the changing dielectric environment. The study uncovers the plausible cause of the layer-dependent electrical conductivity of TMDs.

DOI: [10.1103/PhysRevB.105.165430](https://doi.org/10.1103/PhysRevB.105.165430)

## I. INTRODUCTION

In modern electronics, layered transition metal dichalcogenides (TMDs) such as MoS<sub>2</sub> and WS<sub>2</sub> have attracted a great deal of attention as candidates to replace conventional Si technology [1,2]. The quantum confinement of electrons in two-dimensional (2D) crystal make one-layer (1L) MoS<sub>2</sub> and WS<sub>2</sub> as a direct band-gap semiconductor. Their band structure shows a remarkable evolution with the number of layers, transitioning from direct to indirect as the thickness increases from 1L onwards [3,4]. 1L-MoS<sub>2</sub>(WS<sub>2</sub>)-based FETs exhibit good electrical mobility of  $\sim 200(486) \text{ cm}^2\text{V}^{-1}\text{s}^{-1}$ , however, they show poor mobilities in the bulk phase, which fall in the range of  $\sim 0.3\text{--}0.5 \text{ cm}^2\text{V}^{-1}\text{s}^{-1}$  [2]. Moreover, the electrical conductivity ( $\sigma$ ) of layered MoS<sub>2</sub> and WS<sub>2</sub> increases as the number of layers (NLs) reduces [5–7]. On the other hand, there are conflicting experimental reports on the trend of conductivity with the function of NLs [8–12]. Therefore, the origin of this change in electrical conductivity and mobility is still under debate and remains an open question.

In the crystal structure of bulk TMDs, each 2D layer is bounded by the weak van der Waal's force, which makes it possible to exfoliate a few layers or even a 1L through the various experimental techniques [13–19]. However, none of the existing processes provides the capability to exclusively produce uniform monolayers over a large area [6,20]. Additionally, none of these processes can precisely control the NLs. For example, 1L-MoS<sub>2</sub> and 1L-WS<sub>2</sub> obtained from these processes always coexist with thicker layers [17,20,21]. As the properties of MoS<sub>2</sub> and WS<sub>2</sub> strongly depend on NLs, a controlling number of layers in exfoliated samples remains a tremendous challenge for the improvement of device performance [7,22–25]. As-grown 1L-MoS<sub>2</sub> and 1L-WS<sub>2</sub> are *n*-type

semiconductors because of the unintentional presence of hydrogen during growth [26,27]. Hydrogen in interstitial ( $H_i$ ) and the H-S adatom configuration provide effective shallow donor levels in 1L-MoS<sub>2</sub> [26] and 1L-WS<sub>2</sub> [27]. However, these donor levels are deep in the bulk phase [28], highlighting the tremendous changes in defect behavior as a function of the number of layers.

Using density functional theory, we carried out a comprehensive study of *n*-type ( $H_i$  and H-S adatom) and *p*-type ( $V_S$ ) defects in MoS<sub>2</sub> and WS<sub>2</sub>, from one-layer (1L) to nine-layers (9L) and then in the bulk phase. We found that the shallow donor levels in 1L-MoS<sub>2</sub> and 1L-WS<sub>2</sub>, systematically tuned to deep levels as NLs increase, which reduce the *n*-type conductivity. Interestingly, from eight-layers (8L) onwards, the deep levels shift towards the conduction band and resembles the bulk behavior. On the other hand, sulfur vacancy ( $V_S$ ), which is a deep acceptor in 1L-MoS<sub>2</sub> and 1L-WS<sub>2</sub>, turns out to be a weak shallow acceptor for six-layers (6L). These weak shallow acceptor levels start shifting towards the conduction band after 6L onwards and become deep, and therefore, reduces the *p*-type conductivity. The competition between the bonding characteristics of the defect state, Coulombic interactions of added charge, and dielectric screening determine the layer-dependent behavior of electrical conductivity. The finding suggests that the electrical conductivity can be controlled by adding the NLs of TMDs, without changing their integrity.

## II. METHODOLOGY

Our calculations are based on density functional theory (DFT) within the generalized gradient approximation (GGA) [29–31] and projector augmented wave (PAW) potentials as implemented in the Vienna *ab initio* simulation package (VASP) [32,33]. The kinetic energy cutoff is set to 400 eV for the plane-wave expansion. All the structures are completely relaxed until the components of the Hellmann-Feynman

\* abhishek@iisc.ac.in

forces are less than 0.005 eV/Å. A dense Monkhorst-Pack  $k$ -point,  $21 \times 21 \times 1$  for a unit cell of 1L and  $15 \times 15 \times 11$  for a unit cell of 2L to 9L of MoS<sub>2</sub> and WS<sub>2</sub> is used for the complete geometry optimization.

The defect [X] formation energy in charge state  $q$  is given by

$$E^f[X^q] = E_{\text{tot}}^{\text{defect}} - E_{\text{tot}}^{\text{pristine}} - \sum_i n_i \mu_i + qE_F + \Delta^q, \quad (1)$$

where  $E_{\text{tot}}^{\text{defect}}$  and  $E_{\text{tot}}^{\text{pristine}}$  are the total energies of defective and pristine supercells, respectively.  $n_i$  is the number of atoms of the  $i^{\text{th}}$  species, either added to ( $n_i > 0$ ) or removed ( $n_i < 0$ ) from the pristine supercell.  $\mu_i$  is the chemical potential of the  $i^{\text{th}}$  element.  $E_F$  is the Fermi-level position, referenced to the valence-band maximum (VBM).  $\Delta^q$  represents the charge-state correction due to the finite size of the supercell. To correct the spurious Coulombic interactions, first we converged the defect formation energies as a function of supercell size. We considered sufficiently large supercells, wherein the periodic distance of the charged defect is more than 18 Å. Previous studies [34,35] suggested that in 1L and few-layered MoS<sub>2</sub>(WS<sub>2</sub>), for the lower charge state, i.e.,  $\pm 1$ , the periodic distance 18 Å was sufficient to predict the converged formation energies with an error bar of  $\sim 0.15$  eV. A  $4 \times 4 \times 4$   $k$ -point sampling is used for all the calculations. The significance of the defect transition level (DTL) is explained in the Supplemental Material (SM) [36].

### III. RESULTS AND DISCUSSION

The unit cells of 1L and bulk MoS<sub>2</sub> consist of three and six sublayers in the chalcogen-metal-chalcogen (X-M-X) configuration [1,2]. In order to assess the interlayer coupling strength, we calculate the layer-dependent cohesive energy. The analysis suggests that separating the layers from the bulk requires a large amount of energy, please see Fig. S1 of SM [36]. Few-layered MoS<sub>2</sub> having an even number of layers, has inversion symmetry, which is not present in odd layers. The optimized lattice parameter and interlayer distance are  $a = 3.17$  Å and  $d_{\text{Mo-Mo}} = 6.15$  Å, respectively. This is consistent with the previous experimental reports [1,2,4,37]. The van der Waal's (vdW) interaction is included through the semiempirical Grimme's DFT-D2 [38] formalism. We find that  $a$  and  $d_{\text{Mo-Mo}}$  are independent of the NLs.

The calculated PBE-GGA direct energy gap of 1L-MoS<sub>2</sub> is 1.7 eV, which is very close to the previous experimental value 1.8 eV [1,3,4,37,39]. The VBM at the  $K$ -point is 54 meV higher in energy than the local maximum at  $\Gamma$  for the 1L-MoS<sub>2</sub>, as shown in Fig. S2(a) of the SM [36]. As the number of layers increases, VBM shifts monotonically from  $K$  to  $\Gamma$ , and CBM remains at  $K$ , making it an indirect band-gap semiconductor. From 2L to 6L, the orbitals at  $\Gamma$  (VBM) are composed of metal  $d_{z^2}$  and chalcogen  $p_z$  orbitals, while CBM is composed of only metal  $d_{z^2}$  orbitals. After 7L, CBM starts shifting halfway along the  $\Gamma \rightarrow K$  direction. As the NLs increase, the lowest conduction band moves down reducing the band gap, which reaches to 0.99 eV for the bulk, as shown in Fig. S2(c) of the SM [36]. In bulk MoS<sub>2</sub>, CBM is composed of  $d_{xy}$ ,  $d_{x^2-y^2}$ , and  $d_{z^2}$  orbitals, whereas VBM originates from  $d_{z^2}$  and  $p_z$  orbitals. The band-edge positions of

layered ( $n = 2, \dots, 9$ ) and bulk MoS<sub>2</sub> are shown in Fig. S2(b) of the SM [36]. The band gap monotonically decreases with the NLs and converges to the bulk value, which indicates the effect of quantum confinement [3,40–42].

Hydrogen impurities are frequently observed in MoS<sub>2</sub> due to the use of H<sub>2</sub>S gas as the sulfur source and predicted to be the cause of electron doping [43–45]. We considered hydrogen (H) impurities at different lattice sites in 1L and bulk MoS<sub>2</sub>. After the complete geometrical optimization, hydrogen is found to be the most stable in two different structural configurations; (i) H interstitial H<sub>i</sub>, wherein hydrogen is in the middle of the hexagon center and (ii) H-S adatom with hydrogen on the top of the S atom. For the H<sub>i</sub> configuration, the calculated Mo-H bond length is 1.88 Å, which is close to the experimental value of 1.74 Å. For the H-S adatom configuration, the calculated H-S bond length is 1.34 Å, which is close to the H-S bond length in H<sub>2</sub>S gas. The variation of the bond length and total energy per atom as a function of the number of layers is in the range of  $\sim 0.01$  Å and 0.05 eV, respectively. The H-S adatom is energetically more stable when H stays between the layers rather than on the top layer. The energy difference for these two configurations is  $\sim 0.12$  eV. The H-S bond length remains unchanged in both configurations. Hence, the defect thermodynamic analysis of the H-S adatom is done for the lowest-energy (second) configuration. We also analyzed layer-dependent thermodynamics of the sulfur vacancy ( $V_S$ ), which is one of the most abundant defects in MoS<sub>2</sub> and WS<sub>2</sub> [2,6]. After the geometrical optimization, the three Mo(W) atoms surrounded by the  $V_S$  move 0.13 Å, inward.

The defect transition levels (DTLs) analysis as a function of the Fermi level, of H<sub>i</sub>, H-S adatom, and  $V_S$  in 1L and bulk MoS<sub>2</sub> are shown in Figs. 1(a) and 1(c), respectively. For 1L, the H<sub>i</sub> and H-S adatom provide a shallow donor level and lead to  $n$ -type conductivity under an S-rich condition, as shown in Fig. 1(a). In disagreement with the previous experimental reports [5–7], we found  $V_S$  as an electron acceptor defect and the associated DTL  $\epsilon(0/-1)$  occurs at 1.61 eV (0.68 eV) above the VBM for 1L (bulk) MoS<sub>2</sub>. Under the Mo-rich condition, when the Fermi level approaches to CBM ( $n$ -type doping),  $V_S^{-1}$  is most stable compared to H<sub>i</sub><sup>+1</sup> and the H-S<sup>+1</sup> adatom, which will trap the free carriers and reduces the  $n$ -type conductivity of 1L. Interestingly, H<sub>i</sub>, which is a shallow donor in 1L, turns out to be a deep donor in bulk, as shown in Fig. 1(c). The  $\epsilon(+1/0)$  level occurs 0.31 eV below the calculated CBM or 0.42 eV below the experimental CBM [3]. Moreover, the simultaneous presence of the H-S<sup>+1</sup> adatom donor and  $V_S^{-1}$  acceptor, pins the Fermi level at  $E_F = E_{\text{CBM}} - 0.35$  eV, as shown in Fig. 1(c). The H<sub>i</sub> and H-S adatom both provide midgap states and cannot be the source of the  $n$ -type conductivity of bulk MoS<sub>2</sub>. The DTLs are shallow in 1L and are deep in bulk, therefore, it is important to understand their changes as a function of the number of layers.

We investigate the variation of DTLs of H<sub>i</sub>, and H-S adatom as a function of the number of layers (NLs) of MoS<sub>2</sub> as shown in Fig. 1(b). All the DTLs plotted as a function of Fermi level are shown in Figs. S3 and S4 of the SM [36]. For 2L MoS<sub>2</sub>, the  $\epsilon(+1/0)$  level occurs at 0.25 eV and 0.38 eV below the CBM for H<sub>i</sub> and H-S adatom, respectively. Therefore, shallow donor levels of H<sub>i</sub> and H-S adatom in 1L turns out

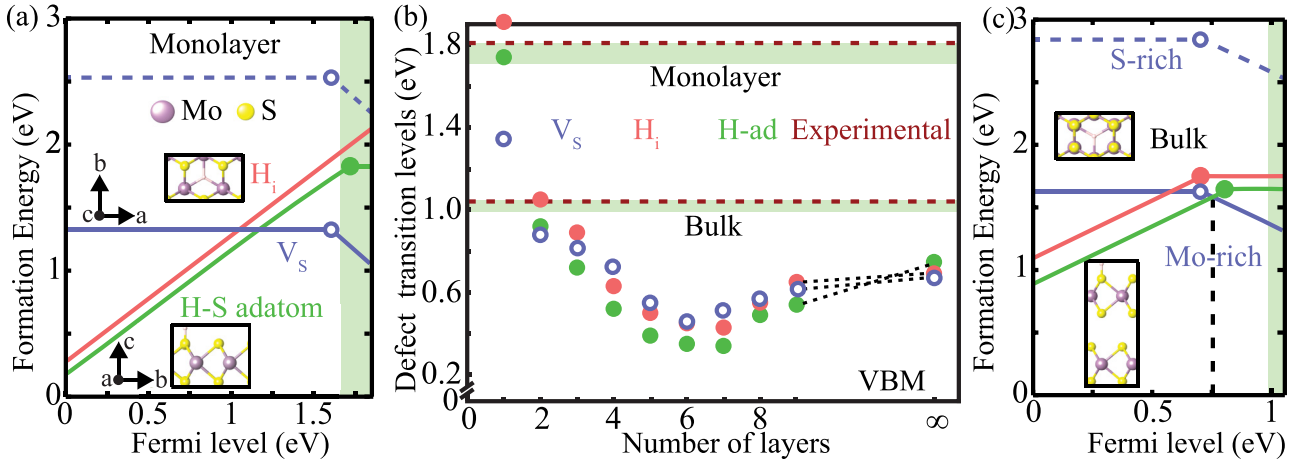


FIG. 1. Defect formation energies as a function of  $E_F$  for  $H_i$ , H-S adatom, and  $V_S$  in (a) 1L, (b) as a function of number of layer, and (c) bulk  $\text{MoS}_2$ . The Fermi level is referenced to the respective VBM. The corresponding optimized structures are shown in the inset. The vertical green shaded region represents the band gap of 1L and bulk  $\text{MoS}_2$  with the calculated value (lower Fermi-level) and experimental value (upper Fermi-level). The vertical black dotted line represents the pinned value of the Fermi level. Solid and dotted horizontal blue color lines represent the formation energy of  $V_S$  in Mo-rich and S-rich conditions, respectively.

to be a deep donor in 2L. The DTLs also shift progressively towards the valence band for 3L onwards. The  $\epsilon(+1/0)$  level for  $H_i$  (H-S adatom) occurs at 0.49 eV (0.32 eV), 0.67 eV (0.56 eV), 0.74 eV (0.63 eV), 0.74 eV (0.64 eV), and 0.73 eV (0.63 eV) below the CBM for 3L, 4L, 5L, 6L, and 7L respectively. The position of the transition levels for 5L, 6L, and 7L remains almost unchanged, as shown in Fig. 1(b). Interestingly, for 8L and 9L, the deep donor levels of  $H_i$  and H-S adatom start shifting towards the conduction band. The  $\epsilon(+1/0)$  level of  $H_i$  (H-S adatom) for 8L and 9L of  $\text{MoS}_2$ , occurs at 0.58 eV (0.50 eV) and 0.50 eV (0.40 eV), respectively. Therefore, the electrical conductivity of  $\text{MoS}_2$  will strongly depend on NLs, and it will start to behave as bulk after 6L or 7L, indicating a nano to bulk transition.

For the 2L- $\text{MoS}_2$ , the  $\epsilon(0/-)$  level of  $V_S$  occurs at 0.88 eV above the VBM, Fig. 1(b). The DTLs as a function of the Fermi level is shown in Fig. S5 of the SM [36]. For the 3L, 4L, 5L, and 6L, the  $\epsilon(0/-)$  levels are located at 0.81 eV, 0.72 eV, 0.55 eV, and 0.46 eV above the VBM, respectively. Interestingly, the hole excitation of  $V_S^0 \rightarrow V_S^{-1} + h^+$ , which requires 1.61 eV in 1L reduces to 0.40 eV in the 6L- $\text{MoS}_2$ . Therefore, 6L- $\text{MoS}_2$  may show weak  $p$ -type conductivity. After the 6L, the  $\epsilon(0/-)$  level starts shifting towards the CBM. For 7L, 8L, and 9L, the  $\epsilon(0/-)$  levels are located at 0.51 eV, 0.57 eV, and 0.61 eV, respectively, above the VBM. The positions of all the DTLs with respect to the vacuum level are summarized in Fig. S2(b) of the SM [36].

We calculate the defect concentrations using the formation energies at the conduction band minima of  $H_i$  and H-ad defects, as they provide  $n$ -type doping to  $\text{MoS}_2$ . We assume the growth temperature to be  $T = 1200$  K for the estimation of defect concentrations. The defect concentrations of  $H_i$  (H-ad) in 1L, 2L, 5L, and bulk  $\text{MoS}_2$  are  $1.2 \times 10^{15} \text{ cm}^{-3}$  ( $1.8 \times 10^{15} \text{ cm}^{-3}$ ),  $2.8 \times 10^{15} \text{ cm}^{-3}$  ( $2.8 \times 10^{15} \text{ cm}^{-3}$ ),  $4.9 \times 10^{15} \text{ cm}^{-3}$  ( $4.9 \times 10^{15} \text{ cm}^{-3}$ ), and  $3.3 \times 10^{14} \text{ cm}^{-3}$  ( $2.8 \times 10^{14} \text{ cm}^{-3}$ ), respectively. The estimated hydrogen impurities concentration is in the range of  $\sim 0.3\text{--}5 \times 10^{15} \text{ cm}^{-3}$

in  $\text{MoS}_2$ . As a hydrogen defect can provide one electron, therefore, the total charge carrier concentrations ( $n_0$ ) will be equal to the total hydrogen impurities' concentration. However, the charge carrier concentrations ( $n_e$ ), which actively contribute to the electrical conductivity, depends on the activation energy ( $E_a$ ) of the defects in their respective charge states (i.e.,  $H_i^{+1}$  and  $H\text{-S}^{+1}$ ). We calculate  $n_e$  through the statistical distribution  $n_e = n_0 \exp(-E_a/k_B T)$ . The  $n_e$  of  $H_i$  (H-ad) are  $1.2 \times 10^{15} \text{ cm}^{-3}$  ( $1.8 \times 10^{15} \text{ cm}^{-3}$ ),  $6.2 \times 10^{14} \text{ cm}^{-3}$  ( $3.7 \times 10^{14} \text{ cm}^{-3}$ ),  $1.5 \times 10^{13} \text{ cm}^{-3}$  ( $3.6 \times 10^{13} \text{ cm}^{-3}$ ), and  $2.85 \times 10^{14} \text{ cm}^{-3}$  ( $2.89 \times 10^{14} \text{ cm}^{-3}$ ) for 1L, 2L, 5L, and bulk, respectively (at a 1200 K growth temperature). We showed the variation of the charge carrier concentration as a function of NLs in Fig. 2, which clearly shows the layer dependence nature of charge carriers and hence the electrical conductivity ( $\sigma$ ). We found that the  $\sigma$  shows the superlinear behavior with the sample thickness ( $t$ ) of  $\text{MoS}_2$ , i.e.,  $\sigma \propto t^{-k}$ , which agrees well with the previous reports [8,12]. Moreover,

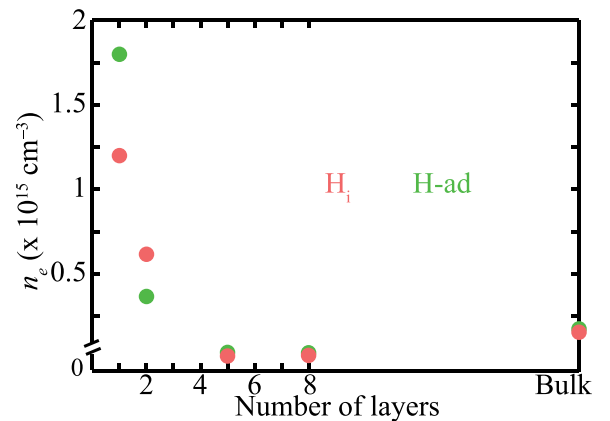


FIG. 2. Variation of electron carrier concentrations provided by  $H_i$  and H-ad defects in layered  $\text{MoS}_2$ , as a function of NLs.

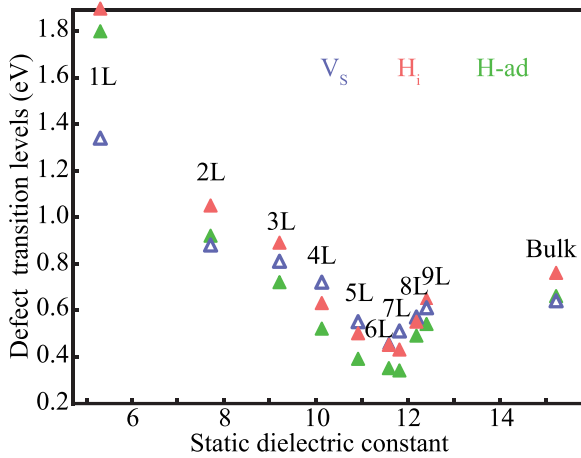


FIG. 3. Variation of DTLs for  $V_S$ ,  $H_i$ , and H-adatom as the function of static dielectric constant in layered  $\text{MoS}_2$ . The open and filled triangle represents the acceptor and donor nature of transition levels.

the thickness-dependent electrical conductivity has commonly been observed in  $\text{MoS}_2$  regardless of the synthesis methods, e.g., mechanical exfoliation [11,46], chemical vapor deposition [10,47], chemical and physical vapor transport [8,12], and so on. Hydrogen is a ubiquitous impurity, present unintentionally in most of these growth environments and acts as a donor defect [26]. Therefore, our study provides an atomistic origin of the layer-dependent conductivity from donor defects in  $\text{MoS}_2$ . We emphasize here that the trend of the electrical conductivity or the value ( $k$ ) of superlinear behavior may differ depending on the amount of donor hydrogen defects present in different growth environments.

To gain physical insights into the layer-dependent properties of these defects, next, we analyzed the variation of the DTLs of layered  $\text{MoS}_2$  as a function of the dielectric constant. Due to the significantly reduced dielectric screening [34,48], the charged defects experience strong Coulomb interactions in 2D layers than the bulk, and hence strongly affect the DTLs. The dielectric constants are calculated using the density functional perturbation theory (DFPT) [49]. The calculated dielectric constant for a supercell  $L_{xyz}$  can be approximated by an average of the dielectric constant for the 2D layer ( $L_{xy}$ ) with the thickness of  $2d_0$  and that for the vacuum region (with a thickness of  $L_z - 2d_0$ ), and given by

$$\varepsilon_{\perp}^{avz} = \frac{2d_0\varepsilon_{\perp} + (L_z - 2d_0) \times 1}{L_z}, \quad (2)$$

where  $\varepsilon_{\perp}$  is the relative dielectric constant of the 2D layer. The variation of transition levels of the  $H_i$ , H-S adatom, and  $V_S$  as a function of the dielectric constant is shown in Fig. 3. In 1L, due to the weak screening and strong quantum confinement,  $V_S$  gives rise to a strongly localized defect state, i.e., deep level. As the NLs increases, the dielectric screening of the charged defects increase, which delocalizes the defect states, thereby the ionization energies of  $V_S^{-1}$  systematically decrease. The same delocalization of defect levels gives rise to an opposite behavior for the donor defects, i.e.,  $H_i$  and H-S adatom, where all the DTLs progressively become deep with

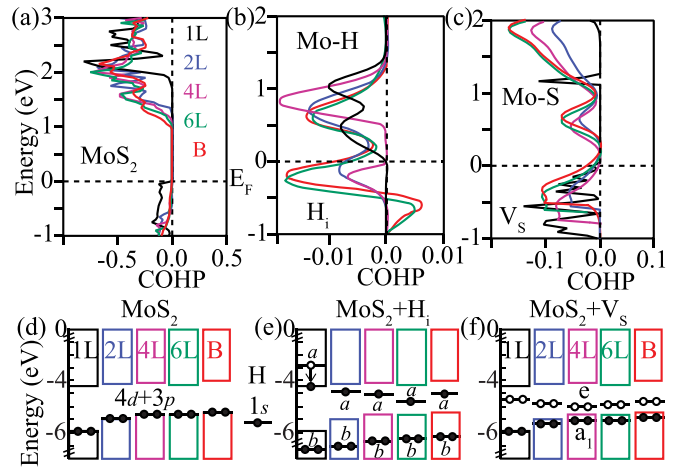


FIG. 4. COHP analysis of (a) layered pristine  $\text{MoS}_2$ , (b)  $H_i$ , and (c)  $V_S$  in  $\text{MoS}_2$ , respectively. Colors represent the respective NLs. Positive and negative  $X$  axis represent the bonding and antibonding nature of states. The vacuum-level-aligned energy diagram of (d) layered  $\text{MoS}_2$ , (e)  $H_i$ , and (f)  $V_S$  in  $\text{MoS}_2$ , respectively.  $a$  and  $b$  represent the antibonding and bonding states. The filled and open circle represents the occupied and unoccupied states, respectively.

the increasing NLs. Interestingly, we found that for both donor and acceptor defects, first DTLs move towards the VBM; subsequently, after 6L or 7L, they all move towards the CBM following the trend in the dielectric constant.

To analyze it further, we study the character of low-energy states and the local bonding near the Fermi level. We calculated the Kohn-Sham levels of  $H_i$ , H-S adatom, and  $V_S$  by using the crystal orbital Hamiltonian population (COHP) [50] shown in Fig. 4. We also analyzed the orbital-resolved electronic density of states (DOS) of  $H_i$  and  $V_S$  in the layered  $\text{MoS}_2$  and summarized in Fig. S6 of the SM [36]. In defect-free 1L to 6L  $\text{MoS}_2$  and the bulk, the frontier occupied and unoccupied orbitals forming the conduction bands are all antibonding types, which are in the negative  $X$ -axis as shown in Fig. 4(a). When an H atom is placed at the interstitial position of 1L  $\text{MoS}_2$ , the H-1s orbital strongly interacts with the occupied  $d_{z^2}$  and  $p_z$  orbitals of VBM, as shown in Fig. 4(e). This interaction forms a bonding state located at  $\sim 3$  eV below the VBM and an antibonding state located at  $\sim 0.8$  eV above the CBM, as shown in Fig. 4(e).

The two of three electrons (one from H-1s and two from the occupied  $d_{z^2}$  and  $p_z$  orbitals) fill the bonding state; the third electron, which would occupy the antibonding state lying high in the conduction bands, is transferred to the CBM, Fig. 4(e). This antibonding transferred electron leads the  $n$ -type conductivity in 1L- $\text{MoS}_2$ . From 2L onwards, the donor level (antibonding state) shifts from the conduction band to inside the gap, while the bonding state remains inside the valence band. As the NLs increase to 6L or 7L, the antibonding and bonding states start to approach the Fermi level and the system minimizes energy in the neutral charge state. In the  $+1$  charge state, the Coulomb repulsion due to the added electron ( $H_i^0 \rightarrow H_i^{+1} + e^-$ ) results in the shift of DTLs towards VBM making it deep, Figs. S3 and S4. Therefore, the  $n$ -type conductivity

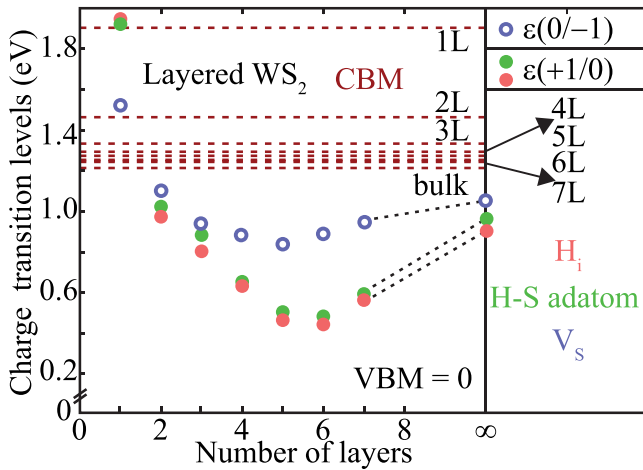


FIG. 5. Variation of defect transition levels as the function of the number of layers of  $\text{WS}_2$ .  $Y$ -axis represents the defect transition levels of  $\text{H}_i$ , H-S adatom, and  $V_S$ , respectively, and the  $X$ -axis represents the NLs. Colors represent their respective defects.  $n = \infty$  represents the bulk limit of  $\text{WS}_2$ .

of  $\text{MoS}_2$  reduces as the number of layers increases. From 8L onwards, CBM starts slowly moving towards high energy. On the other hand, the donor levels (antibonding states) are strongly localized in the band gap, and the bonding states in the valence band are continuously moving to higher energy. The combined effect raises the energy of the neutral charge state of H-interstitial ( $\text{H}_i^0$ ). The significant energy shift of the neutral charge state and minor energy shift of +1 charge state push the DTLs towards the CBM up to the bulk limit, Figs. S3 and S4. The H-S adatom provides an antibonding shallow donor state below CBM for 1L, which was inside the CBM for the case of  $\text{H}_i$ . From 2L onwards, H-S adatom follows the same behavior as  $\text{H}_i$ , i.e., the shifting of DTLs towards the in-gap region initially and then towards the CBM after the 6L.

In the case of  $V_S$  two excess electrons occupy the antibonding state  $a_1$  at the VBM and two unoccupied antibonding states  $e$  located at 1.6 eV above the VBM in the 1L- $\text{MoS}_2$ , Figs. 4(c) and 4(f). The Fermi level is in between the  $a_1$  (deep donor) and  $e$  (deep acceptor) states. As NLs increase up to the 4L or 5L,  $a_1$  and  $e$  states start coming closer to the Fermi level and increase the energy of neutral  $V_S$ . In the  $-1$  charge state, the Coulomb repulsion due to the added valence hole ( $V_S^0 \rightarrow V_S^{-1} + h^+$ ) shifts the DTLs towards the VBM, Fig. S5. Therefore, the deep acceptor level becomes the weak shallow acceptor for the 6L- $\text{MoS}_2$ . From 7L onwards, the acceptor levels shift towards the CBM and the DTLs become deep again. Therefore, as the NLs increase up to 6L, the ionization energy of  $V_S$  decreases and hence increases the  $p$ -type conductivity of  $\text{MoS}_2$ . All the DTLs become deep and hence reduce the  $p$ -type conductivity from 7L onwards up to the bulk limit.

We further investigate the dependence of DTLs as the function of the NLs for  $\text{WS}_2$ . The band gap of  $\text{WS}_2$  varies between 1.9–1.2 eV, as shown in Fig. 5. For 1L- $\text{WS}_2$ ,  $\text{H}_i$ , and H-S adatom provide effective donor levels inside the CB and leads the  $n$ -type conductivity. All the DTLs first shift towards the

VBM, and after 6L, they move towards the CBM, as shown in Fig. 5. For 1L- $\text{WS}_2$ ,  $V_S$  provides a deep acceptor level and DTLs shift with NLs.  $\text{WS}_2$  follows the same behavior as  $\text{MoS}_2$  and shows the layer-dependent electrical conductivity and nano to bulk transition after 6L or 7L. Moreover, due to the similarity in the electronic structure of  $\text{MoS}_2$  with the other layered TMDs such as  $\text{MoSe}_2$ , and  $\text{WSe}_2$ , and so on, the layer-dependent behavior of the DTLs as a function of NLs will be very similar. We note that the electrical conductivity in semiconducting materials is strongly influenced by scattering centers and external stimuli. The ionized impurity scattering limits the mobility of the electrons in  $\text{MoS}_2$  [51]. The presence of the tilted grain boundaries also decreases the electrical conductivity of  $\text{MoS}_2$  [52]. Moreover, the defect levels become shifted inside the gap when the external strain is applied in  $\text{MoS}_2$  [53]. In the present study, we only consider the contribution to the total conductivity from the donor defects only. Therefore, our study will explain the conductivity trend agreeably where the donor defect contribution predominates over other factors.

#### IV. CONCLUSION

In summary, using DFT, we observed that the electrical conductivity of  $\text{MoS}_2$  and  $\text{WS}_2$  is very sensitive to the number of layers (NLs). We investigate the variation of the defect transition levels of  $n$ -type defects, i.e., hydrogen interstitial, H-S adatom, and  $p$ -type defect, i.e., sulfur vacancy as the function of NLs of  $\text{MoS}_2$  and  $\text{WS}_2$ . In 1L, the shallow donor levels of  $\text{H}_i$ , H-S adatom, become deep as the NLs increase to 6L or 7L. The continuous shift of antibonding and bonding states towards the Fermi level lowers the energy of the neutral charge state. Furthermore, the Coulomb repulsion due to the added electron ( $\text{H}_i^0 \rightarrow \text{H}_i^{+1} + e^-$ ) shift DTLs towards VBM, making them deep defects. Interestingly, from 8L onwards, the deep donor levels start shifting towards the conduction band. Moreover,  $V_S$ , which is a deep acceptor in 1L, turns out to be a weak shallow acceptor with the ionization energy of 0.40 eV, for the 6L- $\text{MoS}_2$ . After 6L, DTLs of  $V_S$  start shifting towards the conduction band and become a deep acceptor. Our study provides a comprehensive understanding of the layer-dependent behavior of the key defects in TMDs, thereby settling the long-standing debate on their origin of electrical conductivity.

#### ACKNOWLEDGMENTS

The authors thank the Materials Research Centre (MRC), Solid State and Structural Chemistry Unit (SSCU), and Supercomputer Education and Research Centre (SERC) of the Indian Institute of Science for the computational facilities. This work was supported by the India-Korea Joint Programme of Cooperation in Science and Technology, No. INT/Korea/P-48, Government of India, International Bilateral Cooperation Division. A.S. acknowledges the DST-Inspire fellowship (1F150954). The authors acknowledge the support from the Institute of Eminence (IoE) scheme of The Ministry of Human Resource Development, Government of India.

- [1] K. F. Mak, C. Lee, J. Hone, J. Shan, and T. F. Heinz, Atomically thin MoS<sub>2</sub>: A new direct-gap semiconductor, *Phys. Rev. Lett.* **105**, 136805 (2010).
- [2] B. Radisavljevic, A. Radenovic, J. Brivio, V. Giacometti, and A. Kis, Single-layer MoS<sub>2</sub> transistors, *Nat. Nanotechnol.* **6**, 147 (2011).
- [3] A. Splendiani, L. Sun, Y. Zhang, T. Li, J. Kim, C.-Y. Chim, G. Galli, and F. Wang, Emerging photoluminescence in monolayer MoS<sub>2</sub>, *Nano Lett.* **10**, 1271 (2010).
- [4] R. Ganatra and Q. Zhang, Few-layer MoS<sub>2</sub>: A promising layered semiconductor, *ACS Nano* **8**, 4074 (2014).
- [5] M. Kayyalha, J. Maassen, M. Lundstrom, L. Shi, and Y. P. Chen, Gate-tunable and thickness-dependent electronic and thermoelectric transport in few-layer MoS<sub>2</sub>, *J. Appl. Phys.* **120**, 134305 (2016).
- [6] W. Choi, N. Choudhary, G. H. Han, J. Park, D. Akinwande, and Y. H. Lee, Recent development of two-dimensional transition metal dichalcogenides and their applications, *Mater. Today* **20**, 116 (2017).
- [7] L. Jiao, W. Jie, Z. Yang, Y. Wang, Z. Chen, X. Zhang, W. Tang, Z. Wu, and J. Hao, Layer-dependent photoresponse of 2D MoS<sub>2</sub> films prepared by pulsed laser deposition, *J. Mater. Chem. C* **7**, 2522 (2019).
- [8] M. Siao, W. Shen, R. Chen, Z. Chang, M. Shih, Y. Chiu, and C.-M. Cheng, Two-dimensional electronic transport and surface electron accumulation in MoS<sub>2</sub>, *Nat. Commun.* **9**, 1442 (2018).
- [9] S. Das, H.-Y. Chen, A. V. Penumatcha, and J. Appenzeller, High performance multilayer MoS<sub>2</sub> transistors with scandium contacts, *Nano Lett.* **13**, 100 (2013).
- [10] J. Zheng, X. Yan, Z. Lu, H. Qiu, G. Xu, X. Zhou, P. Wang, X. Pan, K. Liu, and L. Jiao, High-mobility multilayered MoS<sub>2</sub> flakes with low contact resistance grown by chemical vapor deposition, *Adv. Mater.* **29**, 1604540 (2017).
- [11] M.-W. Lin, I. I. Kravchenko, J. Fowlkes, X. Li, A. A. Puzos, C. M. Rouleau, D. B. Geohegan, and K. Xiao, Thickness-dependent charge transport in few-layer MoS<sub>2</sub> field-effect transistors, *Nanotechnology* **27**, 165203 (2016).
- [12] R.-S. Chen, C.-C. Tang, W.-C. Shen, and Y.-S. Huang, Thickness-dependent electrical conductivities and ohmic contacts in transition metal dichalcogenides multilayers, *Nanotechnology* **25**, 415706 (2014).
- [13] S. Manzeli, D. Ovchinnikov, D. Pasquier, O. V. Yazyev, and A. Kis, 2D transition metal dichalcogenides, *Nat. Rev. Mater.* **2**, 17033 (2017).
- [14] S. Tongay, W. Fan, J. Kang, J. Park, U. Koldemir, J. Suh, D. S. Narang, K. Liu, J. Ji, J. Li *et al.*, Tuning interlayer coupling in large-area heterostructures with cvd-grown MoS<sub>2</sub> and WS<sub>2</sub> monolayers, *Nano Lett.* **14**, 3185 (2014).
- [15] N. Perea-López, Z. Lin, N. R. Pradhan, A. Iñiguez-Rábago, A. L. Elías, A. McCreary, J. Lou, P. M. Ajayan, H. Terrones, L. Balicas *et al.*, CVD-grown monolayered MoS<sub>2</sub> as an effective photosensor operating at low-voltage, *2D Mater.* **1**, 011004 (2014).
- [16] G. Collins, K. Nebesny, C. England, L.-K. Chau, P. Lee, B. Parkinson, and N. Armstrong, Orientation and structure of monolayer multilayer phthalocyanine thin films on layered semiconductor MoS<sub>2</sub> and SnS<sub>2</sub> surfaces, *J. Vac. Sci. Technol.* **10**, 2902 (1992).
- [17] J. Sun, X. Li, W. Guo, M. Zhao, X. Fan, Y. Dong, C. Xu, J. Deng, and Y. Fu, Synthesis methods of two-dimensional MoS<sub>2</sub>: A brief review, *Crystals* **7**, 198 (2017).
- [18] M. Pandey, R. Soni, A. Mathur, A. Singh, A. K. Singh, S. Raghavan, and U. Chandni, Noninvasive Subsurface Electrical Probe for Encapsulated Layers in van der Waals Heterostructures, *Phys. Rev. Appl.* **12**, 064032 (2019).
- [19] X. Meng, T. Pandey, J. Jeong, S. Fu, J. Yang, K. Chen, A. Singh, F. He, X. Xu, J. Zhou, W. P. Hsieh, A. K. Singh, J. F. Lin, and Y. Wang, Thermal Conductivity Enhancement in MoS<sub>2</sub> under Extreme Strain, *Phys. Rev. Lett.* **122**, 155901 (2019).
- [20] Y. Yu, C. Li, Y. Liu, L. Su, Y. Zhang, and L. Cao, Controlled scalable synthesis of uniform, high-quality monolayer and few-layer MoS<sub>2</sub> films, *Sci. Rep.* **3**, 1866 (2013).
- [21] A. Sharma, M. A. Verheijen, L. Wu, S. Karwal, V. Vandon, H. C. Knoop, R. S. Sundaram, J. P. Hofmann, W. E. Kessels, and A. A. Bol, Low-temperature plasma-enhanced atomic layer deposition of 2-D MoS<sub>2</sub>: Large area, thickness control and tuneable morphology, *Nanoscale* **10**, 8615 (2018).
- [22] S. Rathi, I. Lee, D. Lim, J. Wang, Y. Ochiai, N. Aoki, K. Watanabe, T. Taniguchi, G.-H. Lee, Y.-J. Yu *et al.*, Tunable electrical and optical characteristics in monolayer graphene and few-layer MoS<sub>2</sub> heterostructure devices, *Nano Lett.* **15**, 5017 (2015).
- [23] Y. Yu, S.-Y. Huang, Y. Li, S. N. Steinmann, W. Yang, and L. Cao, Layer-dependent electrocatalysis of MoS<sub>2</sub> for hydrogen evolution, *Nano Lett.* **14**, 553 (2014).
- [24] X.-L. Li, W.-P. Han, J.-B. Wu, X.-F. Qiao, J. Zhang, and P.-H. Tan, Layer-number dependent optical properties of 2D materials and their application for thickness determination, *Adv. Funct. Mater.* **27**, 1604468 (2017).
- [25] J. Hong, K. Li, C. Jin, X. Zhang, Z. Zhang, and J. Yuan, Layer-dependent anisotropic electronic structure of freestanding quasi-two-dimensional MoS<sub>2</sub>, *Phys. Rev. B* **93**, 075440 (2016).
- [26] A. Singh and A. K. Singh, Origin of *n*-type conductivity of monolayer MoS<sub>2</sub>, *Phys. Rev. B* **99**, 121201(R) (2019).
- [27] A. Singh and A. K. Singh, Atypical behavior of intrinsic defects and promising dopants in two-dimensional WS<sub>2</sub>, *Phys. Rev. Materials* **5**, 084001 (2021).
- [28] Z. Zhu, H. Peelaers, and C. G. Van de Walle, Hydrogen intercalation in MoS<sub>2</sub>, *Phys. Rev. B* **94**, 085426 (2016).
- [29] G. Kresse and J. Furthmüller, Efficient iterative schemes for ab initio total-energy calculations using a plane-wave basis set, *Phys. Rev. B* **54**, 11169 (1996).
- [30] J. P. Perdew, K. Burke, and M. Ernzerhof, Generalized Gradient Approximation Made Simple, *Phys. Rev. Lett.* **77**, 3865 (1996).
- [31] Y. Zhang and W. Yang, Comment on Generalized Gradient Approximation Made Simple, *Phys. Rev. Lett.* **80**, 890 (1998).
- [32] G. Kresse and J. Furthmüller, Efficiency of ab-initio total energy calculations for metals and semiconductors using a plane-wave basis set, *Comput. Mater. Sci.* **6**, 15 (1996).
- [33] M. Fuchs and M. Scheffler, Ab initio pseudopotentials for electronic structure calculations of poly-atomic systems using density-functional theory, *Comput. Phys. Commun.* **119**, 67 (1999).
- [34] J.-Y. Noh, H. Kim, and Y.-S. Kim, Stability and electronic structures of native defects in single-layer MoS<sub>2</sub>, *Phys. Rev. B* **89**, 205417 (2014).

- [35] H.-P. Komsa and A. V. Krasheninnikov, Native defects in bulk and monolayer MoS<sub>2</sub> from first principles, *Phys. Rev. B* **91**, 125304 (2015).
- [36] See Supplemental Material at <http://link.aps.org/supplemental/10.1103/PhysRevB.105.165430> for details of the significance of the defect transition level; layer-dependent cohesive energy of MoS<sub>2</sub>; alignment of defect charge transition levels of H<sub>i</sub>, H-adatom, and V<sub>S</sub>; Layer-dependent defect transition levels of H<sub>i</sub>, H-adatom, and V<sub>S</sub> in layered MoS<sub>2</sub>; And the layer-dependent electronic density of states of MoS<sub>2</sub>.
- [37] X. Li and H. Zhu, Two-dimensional MoS<sub>2</sub>: Properties, preparation, and applications, *Journal of Materiomics* **1**, 33 (2015).
- [38] S. Grimme, Semiempirical GGA-type density functional constructed with a long-range dispersion correction, *J. Comput. Chem.* **27**, 1787 (2006).
- [39] A. Singh, A. Manjanath, and A. K. Singh, Engineering defect transition-levels through the van der waals heterostructure, *J. Phys. Chem. C* **122**, 24475 (2018).
- [40] J. K. Ellis, M. J. Lucero, and G. E. Scuseria, The indirect to direct band gap transition in multilayered MoS<sub>2</sub> as predicted by screened hybrid density functional theory, *Appl. Phys. Lett.* **99**, 261908 (2011).
- [41] A. Kuc, N. Zibouche, and T. Heine, Influence of quantum confinement on the electronic structure of the transition metal sulfide TS<sub>2</sub>, *Phys. Rev. B* **83**, 245213 (2011).
- [42] C. Ataca and S. Ciraci, Functionalization of single-layer MoS<sub>2</sub> honeycomb structures, *J. Phys. Chem. C* **115**, 13303 (2011).
- [43] D. Dumcenco, D. Ovchinnikov, O. L. Sanchez, P. Gillet, D. T. Alexander, S. Lazar, A. Radenovic, and A. Kis, Large-area MoS<sub>2</sub> grown using H<sub>2</sub>S as the sulphur source, *2D Mater.* **2**, 044005 (2015).
- [44] S.-M. Tabatabaei, M.-J. Farshchi-Heydari, M. Asad, and M. Fathipour, Unravelling the physisorption characteristics of H<sub>2</sub>S molecule on biaxially strained single-layer MoS<sub>2</sub>, *Nanoscale Adv.* **1**, 3452 (2019).
- [45] H.-P. Komsa, J. Kotakoski, S. Kurasch, O. Lehtinen, U. Kaiser, and A. V. Krasheninnikov, Two-Dimensional Transition Metal Dichalcogenides under Electron Irradiation: Defect Production and Doping, *Phys. Rev. Lett.* **109**, 035503 (2012).
- [46] R. Dagan, Y. Vaknin, A. Henning, J. Shang, L. Lauhon, and Y. Rosenwaks, Two-dimensional charge carrier distribution in MoS<sub>2</sub> monolayer and multilayers, *Appl. Phys. Lett.* **114**, 101602 (2019).
- [47] J. Jeon, S. K. Jang, S. M. Jeon, G. Yoo, Y. H. Jang, J.-H. Park, and S. Lee, Layer-controlled CVD growth of large-area two-dimensional MoS<sub>2</sub> films, *Nanoscale* **7**, 1688 (2015).
- [48] D. Wang and R. Sundararaman, Layer dependence of defect charge transition levels in two-dimensional materials, *Phys. Rev. B* **101**, 054103 (2020).
- [49] K. Refson, P. R. Tulip, and S. J. Clark, Variational density-functional perturbation theory for dielectrics and lattice dynamics, *Phys. Rev. B* **73**, 155114 (2006).
- [50] V. L. Deringer, A. L. Tchougréeff, and R. Dronskowski, Crystal orbital hamilton population (COHP) analysis as projected from plane-wave basis sets, *J. Phys. Chem. A* **115**, 5461 (2011).
- [51] N. Ma and D. Jena, Charge Scattering and Mobility in Atomically Thin Semiconductors, *Phys. Rev. X* **4**, 011043 (2014).
- [52] A. M. Van Der Zande, P. Y. Huang, D. A. Chenet, T. C. Berkelbach, Y. You, G.-H. Lee, T. F. Heinz, D. R. Reichman, D. A. Muller, and J. C. Hone, Grains and grain boundaries in highly crystalline monolayer molybdenum disulphide, *Nat. Mater.* **12**, 554 (2013).
- [53] M. G. Sensoy, D. Vinichenko, W. Chen, C. M. Friend, and E. Kaxiras, Strain effects on the behavior of isolated and paired sulfur vacancy defects in monolayer MoS<sub>2</sub>, *Phys. Rev. B* **95**, 014106 (2017).